Solid Freeform Fabrication 2024: Proceedings of the 35th Annual International Solid Freeform Fabrication Symposium – An Additive Manufacturing Conference
Reviewed Paper

Physics-based Modeling of Polymer-Metal Composites in Fused Filament Fabrication

Tyler Paupst, Paromita Nath*

Department of Mechanical Engineering, Rowan University, Glassboro, NJ 08028, USA

Abstract

Manufacturing polymer-metal composite products of desired quality using fused filament fabrication (FFF) technologies requires a comprehensive understanding of the material and the process. There has been a substantial effort in recent years on modeling polymer FFF, however, polymer-metal composites exhibit unique physical behaviors. These unique conditions, such as particle-fluid interactions and visco-elastic effects on melt flow, complicate simulation dynamics rendering existing modeling methods ineffective in predicting the melt behavior. This work leverages a computational fluid dynamics modeling approach to simulate the deposition of a homogeneous polymer-metal composite in the FFF process. This approach allows for an efficient investigation of the effects of the process parameters, such as nozzle temperature, print speed, and material composition, on the application-relevant quality of the deposited material. Quantities of interest such as the profile of the deposition and the thermal history are studied. Future considerations for a heterogeneous simulation are also discussed.

Keyword: Computational Fluid Dynamics, Fused Filament Fabrication, Polymer-Metal Composites, Metal Additive Manufacturing

Introduction

Fused filament fabrication (FFF) is a widely available additive manufacturing technology which has experienced significant advancements in recent years. [1] Metal fused filament fabrication (mFFF) is a relatively new development that expands the manufacturing capability of FFF from thermoplastics to composite metal-polymer materials. mFFF provides a cheaper alternative for the additive manufacturing (AM) of metals, compared to other AM technologies for metals such as directed energy deposition (DED) and powder bed fusion (PBF). [2] However, a thorough understanding of the mFFF process is necessary to enable widespread application of this technique. In the mFFF process, metal-polymer composites are used as filaments. Composites with a low metal powder content (20% or less) as particle reinforcement in the polymer matrix are typically unaffected by inter-particle interaction, and the metal-polymer composite maintains its heterogeneous, particle-polymer structure [3]. The material properties of these filaments are generally dominated by their polymer components and are used as printed. However, parts

*Corresponding author. Paromita Nath, Mechanical Engineering, Rowan University, Glassboro, NJ 08028, USA. E-mail: nath@rowan.edu.

manufactured using filaments with high metal content ($\geq 60\%$) undergo the print-debind-sinter (PDS) process, also known as shape-debind-sinter (SDS) [2, 4], similar to the process used in metal injection molding [5]. The PDS process involves printing a part, removing the polymer binder, and then sintering the part to fuse the metal particles, resulting in a strong and dense final product. In such parts, the defects that originate during the printing phase evolve during the remainder of the PDS process. The print step significantly influences the development of the pore structure used for material extraction during the debinding step, and can alter the micro-structure after the sintering step [6, 7]. The densification which occurs during the sintering step is a result of thermally activated diffusion. This leads to significant stress concentrations within the part around induced defects [8], leading to reduced strength of the manufactured part. For further information, a comprehensive review of mFFF process can be found in Bankapalli [9] and Costa [10].

The quality of the printed part is dependent on the melt behaviour and thermal history of the deposited material [11]. FFF process parameters such as print temperature, print speed, build plate temperature and layer thickness influence the melt behavior of the material and subsequently of the temperature gradient and shape of the deposited raster. The shape of the raster determines the contact area between deposited material, which then affects the macro-scale part strength [12, 13]. Studying the relationship between process parameters and the macro-scale quality and properties of additively manufactured parts through experimental means is generally resource-intensive. Thus, a physics model-based approach provides a feasible alternative. Most of the available literature on modeling of FFF processes focuses on polymeric materials. Rashid et al. [14] provides a review of some numerical models for FFF using polymer filaments. Since the majority of phase change in FFF process occurs in the nozzle assembly, modeling of the thermal-kinematic behavior of the polymer is imperative for optimization of process parameters to improve product quality. Thus, numerous efforts [15–18] have been made in modeling liquefier dynamics to analyze melt flow behavior. The current state of numeric modeling for the FFF process predominantly focuses on homogeneous polymers [1, 19, 20]. However, metal-polymer composite filaments require consideration of unique physical interactions compared to polymer FFF, and thus has necessitated the development of models to study the FFF process using these materials.

While the mechanics of the PDS process for mFFF are complex, the print phase is equivalent to FFF process with polymers [5]. However, the interaction between the metal particles and the polymer binder need to be considered, to accurately capture the melt behavior. The coupled interactions between the metal and polymer produce notable effects on the melt flow behavior. The use of particle reinforcement can lead to dimensional inaccuracies due to the difference in thermal behavior of the reinforcement and polymer material. Metal reinforced filaments are frequently subject to significant shrinkage due to thermal gradients present in the deposited material. As metals have substantially higher thermal conductivity and specific heat capacity than the polymer they are reinforcing, the metal particles have a secondary effect on the thermal stresses present in the deposited material. Most studies aimed at understanding the mFFF process are based on experimental investigations [21, 22]. The development of physics-based models remains at a nascent stage. Thus, the adaptation of available research in similar processes, such as metal injection molding, is critical to gain a better understanding of the the mFFF process in an efficient manner [3]. As injection molding is dependent on similar rheological behavior as FFF, many of the approaches used to simulate metal powder injection molding can be considered analogous to the mFFF process [23].

In this work, a physics-based model is developed using computational fluid dynamics (CFD) to the study the melt characteristics in the print phase of the mFFF process. For homogeneous metal-polymer composite filaments with high metal content, the effect of the process parameters such as print speed on the raster shape and temperature gradient is investigated. This work lays the foundation for modeling of mFFF process. The remainder of this paper is organized as follows. Section "Physics-based model of the mFFF print process" describes the modeling of thermal behavior of the metal-polymer material in the mFFF process, including the assumptions and approximations. The implementation of proposed thermal model on an example problem and its results are discussed in the Results and Discussion section. The Conclusion and Future Work section contains the major conclusions and plans for future work.

Physics-based model of the mFFF print process

In this section the computational domain considered to study the mFFF process, determination of the material properties of the composite, and the governing physics for the melt mechanism in the print phase of the mFFF process are discussed.

Computational Domain

The domain considered for simulating the melt behavior of a metal-polymer composite is representative of a single raster deposition on a heated build plate. The nozzle remains fixed in space, while the build plate moves in the Y direction with a constant velocity as shown in Figure 1. A cylindrical fluid source is simulated with a radius r_{SOR} and a height l_{SOR}, to represent the physical influx of molten filament. This source generates fluid at temperature T_f with a total volumetric flow rate, V_f. The pressure and fluid displacement resulting from filament entering the melt region is a driving component of melt behavior inside the nozzle, creating a small re-circulation region. [24, 25]

The previously described effects of the filament supply can be generalized at the nozzle orifice, as the geometry of the melt region in commercially available hot-ends is typically designed to mitigate these effects. Thus, the nozzle region is assumed to have a uniform temperature profile and laminar flow inside the nozzle. (Note that a comprehensive model needs to consider the more complicated underlying heat transfer mechanisms that drive the melt quality [25, 26]). A simplified cylindrical shape is considered for the nozzle geometry to reduce simulation time. The nozzle is approximated as a hollow brass cylinder with an internal diameter of r_N. The length of the inside of the cylinder is defined as l_N. In the physical process, the geometry of the interior cavity of the nozzle is dependent on considerations for maximum flow rate, as the geometry of the hot-end's melt region is responsible for reducing thermal and kinematic turbulence. In the simulation, this length of the internal cavity is based on the equalization region inside the nozzle to ensure errors due to fluid generation do not affect the flow profile as it exits the nozzle. The nozzle is set for a standoff distance (i.e., the intended layer height) of l_{SD}. The build plate is defined as the Z boundary of the domain (see Figure 1). This boundary is defined as a "wall", in which the fluid has physical collision with the surface. The build plate temperature is kept at a uniform T_B. The heat transfer coefficient between the wall and fluid is defined as h_{Wall}.

To reduce computation complexity, the fluid and metal particles are assumed to form a

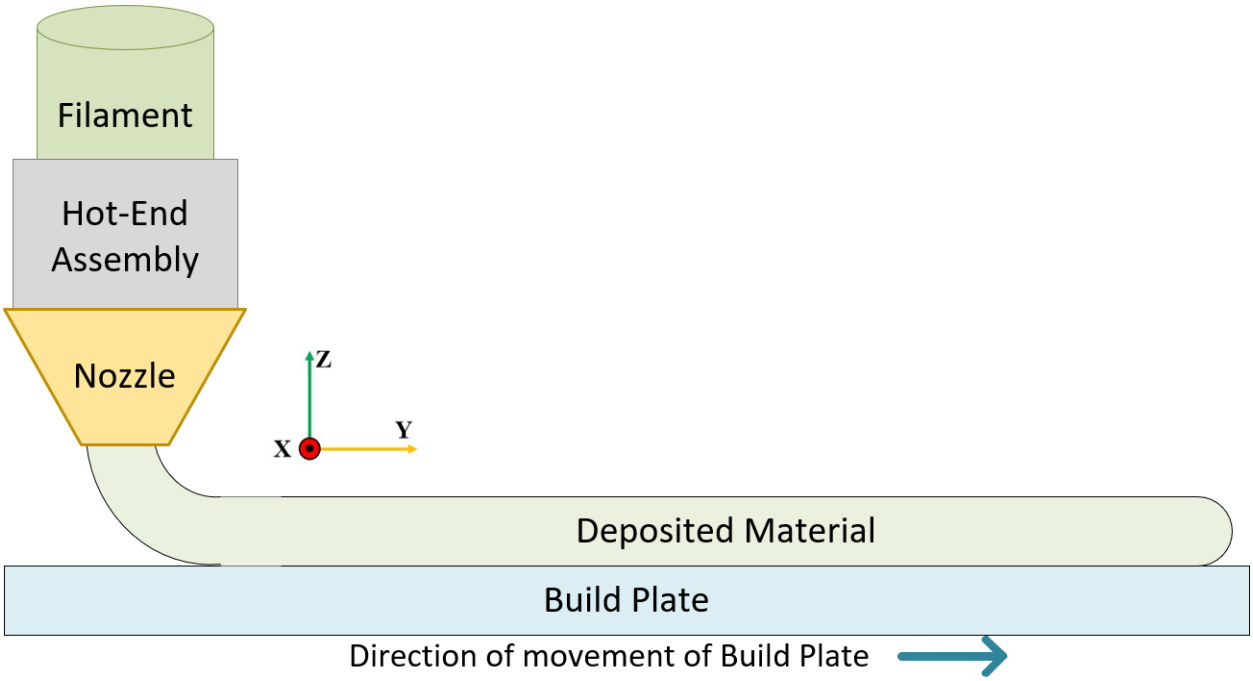

Figure 1: Schematic view of the simulated mFFF process, where the build plate moves in the y direction.

homogeneous mixture. This provides sufficient detail on the macro-scale material properties of the filament with reasonable computational effort. The approximation of the particle-bound polymer as a homogeneous structure is a common approach used in powder injection molding. Based on guidelines presented in [27], the theoretical filament properties are calculated using the rule of mixtures, based on the volume percentage contribution of the material. As the final melt properties of metal-polymer composites are dependent on the ratio of the constituent materials, the properties of the composite can be estimated when the these properties are not available in the literature or database. The material approximations for the FFF filament are assumed to be similar to the metal injection molding feedstock, and are approximated through the rule of mixtures approach. The properties of a composite material (A_f) can be approximated from its constituent materials and their respective volume fractions as shown in Eq. 1 .

$$A_f = A_b + \psi(A_m - A_b) \tag{1}$$

where A_b represents the thermal property of the pure binder, A_m represents the property of the pure metal powder, and ψ represents the volume fraction of the powder. For example, equation 1 can be rewritten to calculate the density and thermal conductivity of the material. The specific heat capacity is estimated through a modified rule of mixtures [27, 28] given by Eq. 2.

$$C_{p_f} = \left[C_{p_b}X_b + C_{p_p}X_p\right] * \left[1 + A * X_b X_p\right] \tag{2}$$

where C_{p_f} is the filament's specific heat, C_{p_b} is the binder's specific heat, C_{p_p} is the metal powder's specific heat, A is a constant dependent on powder shape (0.2 for spherical powders), and X_b and X_p are the binder and powder volume fractions. For more information on this approximation see reference [27].

Computational Fluid Dynamics Model

Computational fluid dynamics (CFD) is applied to analyze the computational domain of mFFF process described in the previous subsection. In this work, the commercial software FLOW-3D [29] is utilized. The physics involved in the mFFF process is briefly described below. For more information, see Ref. [29].

The model considers conservation of mass, momentum and energy. Mass continuity (Eq. 3) ensures that no mass can created or destroyed. Thus, all fluid that enters and exits the simulated domain is accounted for.

$$V_F \frac{\partial \rho}{\partial t} + \frac{\partial}{\partial x}(\rho u A_x) + \frac{\partial}{\partial y}(\rho v A_y) + \frac{\partial}{\partial z}(\rho w A_z) = R_{DIF} + R_{SOR} \tag{3}$$

where V_F represents the fluid volume fraction open to flow, ρ is the density of the primary fluid, R_{DIF} represents a turbulent diffusion term, and R_{SOR} represents the mass source. The fractional areas (A_x, A_y, A_Z), denote the area of the cell open to flow with respect to the direction of it's respective axis.

In order to satisfy conservation of momentum, the calculation of the fluid velocity components *(u,v,w)* in the three Cartesian directions is performed through a modified version of Navier-Stokes equations, seen in Eqs. 4, 5, and 6.

$$\frac{\partial u}{\partial t} + \frac{1}{V_F}\left\{ u A_x \frac{\partial u}{\partial x} + v A_y \frac{\partial u}{\partial y} + w A_z \frac{\partial u}{\partial z} \right\} = -\frac{1}{\rho}\frac{\partial p}{\partial x} + G_x + f_x - \frac{R_{SOR}}{\rho V_F}(u - u_w - \delta u_s) \tag{4}$$

$$\frac{\partial v}{\partial t} + \frac{1}{V_F}\left\{ u A_x \frac{\partial v}{\partial x} + v A_y \frac{\partial v}{\partial y} + w A_z \frac{\partial v}{\partial z} \right\} = -\frac{1}{\rho}\left(\frac{\partial p}{\partial y}\right) + G_y + f_y - \frac{R_{SOR}}{\rho V_F}(v - v_w - \delta v_s) \tag{5}$$

$$\frac{\partial w}{\partial t} + \frac{1}{V_F}\left\{ u A_x \frac{\partial w}{\partial x} + v A_y \frac{\partial w}{\partial y} + w A_z \frac{\partial w}{\partial z} \right\} = -\frac{1}{\rho}\frac{\partial p}{\partial z} + G_z + f_z - \frac{R_{SOR}}{\rho V_F}(w - w_w - \delta w_s) \tag{6}$$

For the above momentum equations, (G_x, G_y, G_z) represent body accelerations, (f_x, f_y, f_z) represent viscous accelerations. The R_{SOR} terms represent the injection of the mass at a source, represented by a geometric component. The term $\mathbf{U}_w = (u_w, v_w, w_w)$ represents the velocity of the source component. The velocity of the fluid at the surface of the source relative to the source itself, is represented using $\mathbf{U}_s = (u_s, v_s, w_s)$. The final term δ is used to evaluate the effect of pressure from the fluid source. For fluid sources which generate fluid under the stagnation pressure type, $\delta = 0$. For fluid sources in which the source exhibits static pressure, then $\delta = 1$. As this work assumes stagnation pressure within the nozzle source, $\delta = 0$.

Fluid interfaces are calculated through a volume of fluid (VOF) function [30]. Equation 7 represents the volume of the fluid per unit volume, where F_{DIR} is defined in Eq. 8.

$$\frac{\partial F}{\partial t} + \frac{1}{V_F}\left[\frac{\partial}{\partial x}(F A_x u) + \frac{\partial}{\partial y}(F A_y v) + \frac{\partial}{\partial z}(F A_z w) \right] = F_{DIR} + F_{SOR} \tag{7}$$

$$F_{DIR} = \frac{1}{V_F}\left\{ \frac{\partial}{\partial x}(v_F A_x \frac{\partial F}{\partial x}) + \frac{\partial}{\partial y}(v_F A_y R \frac{\partial F}{\partial y}) + \frac{\partial}{\partial z}(v_F A_z \frac{\partial F}{\partial z}) \right\} \tag{8}$$

In single fluid simulations, F can be interpreted as the volume fraction of the fluid where $F = 1$ represents a cell volume full of fluid, and $F = 0$ represents a cell volume devoid of fluid. The voids are considered as regions filled with a gas with negligible density in comparison to the fluid density.

The diffusion coefficient is defined as $v_F = c_F \frac{\mu}{\rho}$, where c_F is a constant that is the reciprocal of the turbulent Schmidt number. For the purpose of this work, this diffusion term is excluded as the effects of the fluid on it's surrounding environment is not considered.

The thermal flow inside the fluid is calculated through the internal fluid energy Eq. 9, where **I** represents the overall fluid internal energy.

$$V_F \frac{\partial}{\partial t}(\rho I) + \frac{\partial}{\partial x}(\rho I u A_x) + R\frac{\partial}{\partial y}(\rho I v A_y) + \frac{\partial}{\partial z}(\rho I w A_z) = \\ - p\left\{\frac{\partial u A_x}{\partial x} + \frac{\partial v A_y}{\partial y} + \frac{\partial w A_z}{\partial z}\right\} + RI_{DIF} + T_{DIF} + RI_{SOR} \quad (9)$$

For this work, fluid thermal energy is assumed to be a piece-wise linear function of temperature, seen in Eq. 10. T_i and $C_V(T_i)$ denote the temperature and specific heat values in the tabular definition of $C_V(T)$ and N such that $T_{N-1} < T \leq T_N$. As the presented work assumes a constant specific heat value, this can be simplified to $I(T) = C_V(T_1)T_1$.

$$I(T) = C_V(T_1)T_1 + \sum_{i=2,N} 0.5\left[C_V(T_{i-1}) + C_V(T_i)\right](T - T_{i-1}) \quad (10)$$

The described modeling approach for fluid thermal energy accounts for two thermal diffusion modes. RI_{DIF}, seen in Eq. 11, which represents the turbulent diffusion of I and T_{DIF}, seen in Eq. 12, which represents heat conduction. The coefficient in Eq. 11, v_I is equal to $(c_I \mu)/\rho$, where c_I is a reciprocal of the Prandtl number. For Eq. 12 Thermal conductivity, k can be directly specified. If the Prandtl number C_T is specified, the thermal conductivity is defined as $k = (\mu C_v)/C_T$.

$$RI_{DIF} = \frac{\partial}{\partial x}\left(v_I A_x \frac{\partial \rho I}{\partial x}\right) + R\frac{\partial}{\partial y}\left(v_I A_y \frac{\partial \rho I}{\partial y}\right) + \frac{\partial}{\partial z}\left(v_I A_z \frac{\partial \rho I}{\partial z}\right) \quad (11)$$

$$T_{DIF} = \frac{\partial}{\partial x}\left(k A_x \frac{\partial T}{\partial x}\right) + \frac{\partial}{\partial y}\left(k A_y R \frac{\partial T}{\partial y}\right) + \frac{\partial}{\partial z}\left(k A_z \frac{\partial T}{\partial z}\right) \quad (12)$$

The RI_{SOR} term represents the energy source, which is coupled with the mass source R_{SOR}. The fluid source in the model is defined to maintain a user defined temperature. The local heat transfer, q, between the walls of the domain, such as the build-plate, and the fluid is evaluated as a function of wall temperature in the linear relationship shown in Eq. 13.

$$q = hW_A(T_w - T) \quad (13)$$

The heat transfer coefficient, h, can be specified or evaluated through correlation functions based on local conditions. T is the fluid surface temperature, W_A is the heat structure surface area, and

TT_w is the heat-structure (wall) surface temperature.

The above equations are applied at the boundaries of each cell within the computational mesh. This creates a point field of approximated properties. Equation 7 provides the estimate for the % of volume of the cell occupied by the fluid. Equation 4, 5, and 6 provide a summary of accelerations and velocities present within the fluid. Finally, Eqs. 10, 11, and 12 estimate the thermal state of the fluid within each cell. The geometry of the deposited raster (i.e., the width and height) and the temperature profile for the raster is extracted from the result file (.flsgrf) of the FLOW-3D software, using commercial post processing software FLOW-3D POST. The following section applies this model to a homogeneous metal-polymer composite.

Results and Discussion

The computational model discussed in the previous section Computational Fluid Dynamics Model is implemented to study the effect of print speed on the raster shape of a stainless steel (SS) metal-polymer composite. The effect of the different process parameter settings, specifically the print speed, on the thermal gradient and deposition quality is also evaluated. The composite is assumed to be composed of 88% SS 316L metal powder, 6% polyoxymethylene (POM), and 6% polypropylene, which is a mixture used in MIM [27]. The material properties of the constituent materials are provided in Table 1. The properties of the composite is estimated using modified rule of mixtures (Eqs. 1 & 2).

Material / Property	316L	POM	PP	Polymer-Metal
Density (kg/m^3)	8000	1410	1040	7187
Bulk Modulus (GPa)	152	2.5	1.5	134
Thermal Conductivity (W/mk)	16	0.41	0.21	2.053
Specific Heat Capacity $(kJ/kg/k)$	0.847	0.152		0.9266

Table 1: Assumed material properties applied to the simulated metal-polymer composite.

The parameters of nozzle used in this example are based on a standard nozzle of internal radius (r_N) 0.4 mm. For an assumed volumetric flow rate (V_{fluid}) of $2.5mm^3/s$, the height of the internal cavity, l_N is set to 1.2 mm. The height and radius of the cylindrical fluid source is considered to be $r_{SOR} = 0.15$ mm and $l_{SOR} = 0.3$ mm, respectively. The desired layer height or nozzle standoff distance, l_{SD}, is 0.2 mm. The build plate temperature, T_B is set to 50° C, while the ambient temperature is considered to be 20° C. The print speed is set to 10 mm/s, 20 mm/s, 30 mm/s, and 50 mm/s to study its impact on the deposition characteristics. The computational domain consists of a 4 $mm \times 17$ $mm \times 4.2$ mm region, where the width and height, 4 mm and 4.2 mm respectively are the minimum dimensions needed to resolve the simulation without any effect of domain boundaries. The length of the domain, 17 mm is dependent on the property to be investigated. The length was chosen to be 17 mm as it provides sufficient distance in front of the nozzle for observation of re-circulation and allows for observation of a fully developed material flow in the direction of deposition. Using the material parameters and process settings discussed earlier, the model developed in the " Computational Fluid Dynamics Model" section for FFF

process of metal-polymer composites is implemented using the commercially available software FLOW-3D. A global mesh size of 0.1 *mm* is evaluated at a minimum time step of 3×10^{-10}s. The software simulated 3 seconds of time to ensure the deposited material crosses the boundary for all print speeds. The computational time for each simulation is $\approx$ 160 hours (on an average for the different print speeds). The simulations were conducted on a Lenovo P360 workstation with the following components - CPU: Intel Core i9-12900, GPU: NVIDIA RTX A4500, RAM: 128GB 3600 MHz.

For the single layer, single line (raster) simulation (Figure 1), the deposition characteristics are studied at four cross sections in the XZ plane, along the length of the raster in the Y axis at a distance of 0.4 *mm*, 1 *mm*, 2 *mm*, 10 *mm* from the center of the nozzle (see Figure 2).

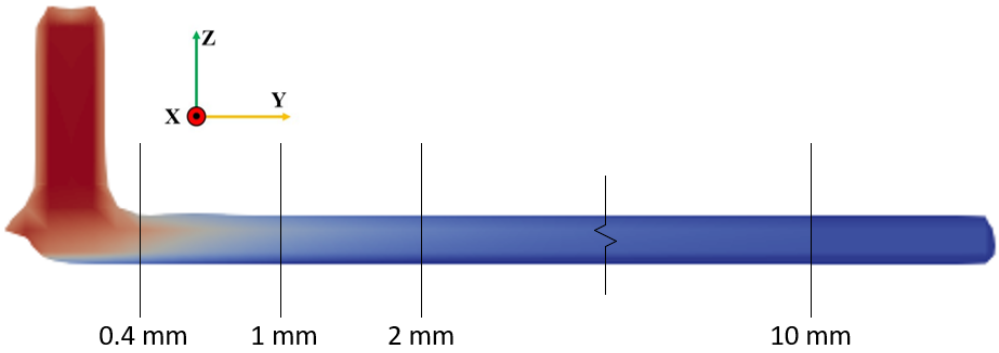

Figure 2: A YZ view of the 20 mm/s deposition where the thermal gradient represents temperature. The labeled distances represent the locations of evaluated cross sections from the nozzle center.

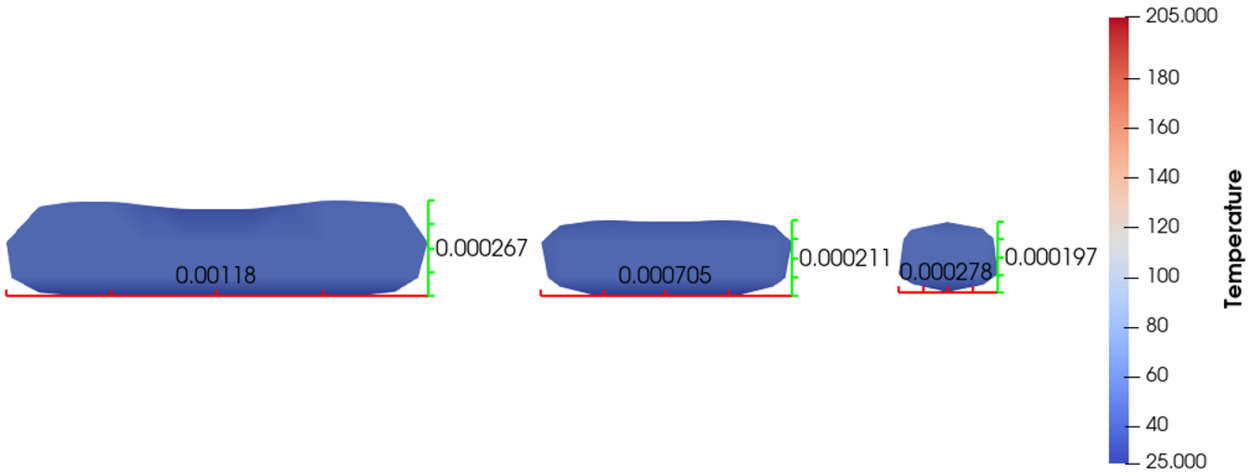

Figure 3: XZ View of simulated depositions 10 mm from the nozzle center for different print speeds. The color gradient represents temperature. Left: 10 mm/s, Center: 30 mm/s, Right: 50 mm/s

At each cross section, the height and width of the raster is estimated. Since the raster cross sections at all speeds are not uniform, as observed in the cross section comparison in Figure 3, the mean value of the raster height and raster width across the cross section is calculated. Figure 3 shows the deposition of various simulated speeds at 10 *mm* from the center of the nozzle. At 10 *mm* the deposition has cooled down, providing an estimate for the final shape of the material.

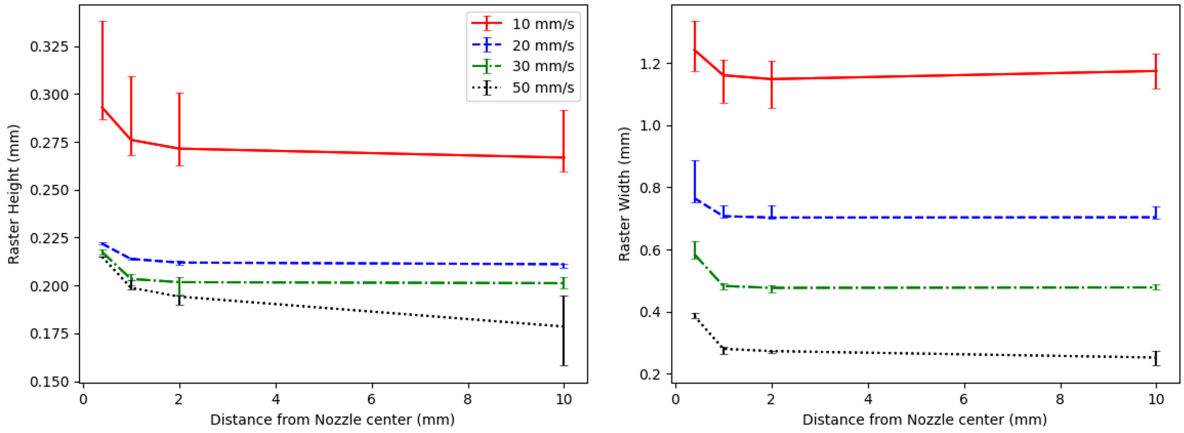

Figure 4: The dimensions of the raster at various print speeds - Height of the raster (left), Width of the raster (right). Error bars represent maximum and minimum dimensions across the cross section.

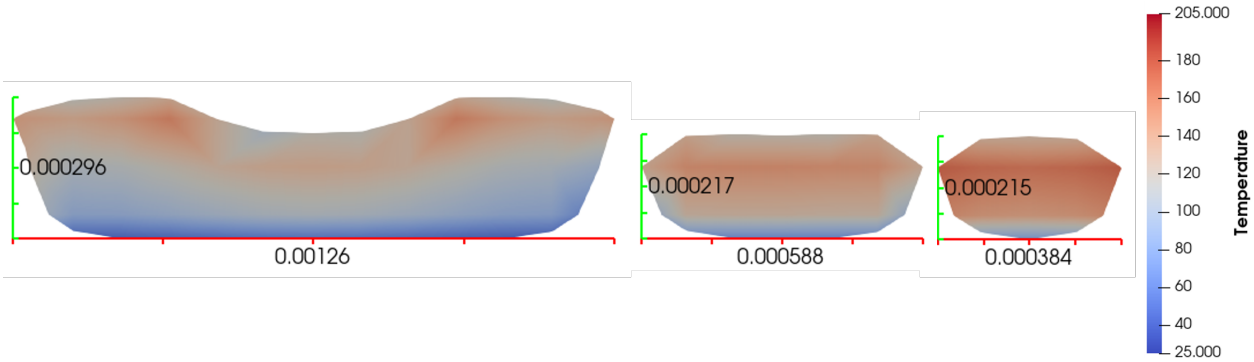

Figure 5: XZ View of simulated depositions at 0.4 mm from the nozzle center for different print speeds. The color gradient represents temperature. Left: 10 mm/s, Center: 30 mm/s, Right: 50 mm/s

Figure 4 shows the variation of raster width and raster height along the length of the raster for the four print speeds. The error bars in the figures indicate the range (minimum and maximum values) of the raster dimensions. From Figure 4 it can be observed that at the lowest and fastest print speeds, the raster shape is not uniform. For the slowest print speed of 10 mm/s, the raster has an average width of 1.174 mm $(+0.056, -0.054)$ and a height of 0.267 mm $(+0.007, -0.025)$. The fastest speed (50 mm/s) deposited material with a width of 0.253 mm $(+0.026, -0.020)$ mm and a height of 0.178 mm $(+0.020, -0.016)$. It can also be observed that the variation in the geometry is lower, as reflected by the error bars, at print speeds of 20 mm/s and 30 mm/s. Since the print speed affects the raster shape, and the raster shape impacts the part geometry and quality, these results indicate the need for optimization of process parameters. Using physics-based models for optimization will reduce the wastage of material incurred in trial-and-error method of experiment-based process parameter optimization.

In order to gain an understanding of the variation in the cross sectional dimensions of the raster along its length at the different print speeds, the thermal gradients are studied. The temperature profile along the X and Z direction for each XZ cross section is obtained for all print speeds. For

reference, the temperature profile of the 20 mm/s along the Y direction the nozzle is plotted in Figure 2. Figure 5 details the XZ cross section of the deposition at 0.4 *mm* from the nozzle center. The temperature profile at this distance is approximated to be the "as printed" temperature profile, i.e., immediately after the material is deposited. For slower speeds such as 10 mm/s, the majority of cooling occurs immediately after deposition (before the 1 *mm* cross section). For the fastest speed ($50 mm/s$) the deposited material retains heat even when the nozzle has moved away further. The increased area of higher temperatures can be advantageous or detrimental to the part-scale process. If the next or adjacent layer is deposited before the current layer cools, the residual heat benefits diffusion across layer boundaries. If the deposited layer is allowed to cool to ambient temperature, the increased area of higher temperature leads to increased thermal shrinkage and decreases interfacial bond strength. The increased thermal shrinkage coupled with an insufficient volumetric flow rate, is assumed to be the reason for the circular deposition shape at 50 mm/s. It is worth noting that the significant error seen for the for the height of the 50 mm/s extrusion at 10 mm from the nozzle is attributed to additional error which occurred due to a restart of the simulation at 2.6s of the intended 3 second simulation time. It is unlikely the error will be present in a continuous run of the simulation.

It is observed in Figure 5 that the print speed has a notable effect on the intensity of the thermal gradient across the deposition. The slower print speeds demonstrate a less severe internal thermal gradient than the faster print speeds. Extreme thermal gradients in deposited filament can weaken interfacial bonds due to an increase in residual thermal stresses, reducing overall part strength [31]. This difference in thermal properties between the metal powder and polymeric binders has a notable contribution to the residual thermal stresses [32]. Such effects need to be considered in multi-line, multi-layer depositions to reduce the defects due to thermal stresses.

Conclusion and Future Work

This work presents an approach for physics-based modeling of melt flow in FFF with metal-polymer composites based on MIM with similar assumptions. The proposed model is implemented to simulate the printing phase of mFFF for a single raster deposition of stainless steel 316L-polyoxymethylene-polypropylene material. The raster shape of and the temperature gradients present in the deposited material are estimated at various spatial locations for different print speeds. It is observed that the slower print speeds ($10 mm/s$ and $20 mm/s$) lead to inconsistent and wider deposition shape, however allows for a slower diffusion of heat inside the fluid, leading to a more uniform temperature profile. Similarly, the faster print speed ($50 mm/s$) resulted in an inconsistent, but circular deposition shape. Due to the rate of deposition, the average temperature of the $50 mm/s$ deposition as printed is notably higher than the average temperature of the $10 mm/s$ deposition. The observed variation in deposition shape at high and low speeds suggest the need for optimization of print speed to achieve the desired geometry of the part. In regards to thermal effects, the fastest print speed required more time to cool to ambient temperature. This suggests that faster print speeds will be subject to sharper thermal gradients when exposed to ambient temperature. The changes in the thermal profile of the deposition indicate that control of heat flux across the deposited fluid is essential to reduce defects such as thermal warping. The similarity of deposition behavior between the simulated material and previous literature of pure polymer models, suggest that it may be feasible to use pre-existing models for macro-scale part simulation.

The validity of the homogeneous assumption must be further evaluated through experimental means.

The above conclusions are based on the proposed model for mFFF and serve as a preliminary step towards forming a comprehensive understanding of thermal behavior of metal-polymer composites. The model needs refinement to be a better representation of the mFFF process. In order to accurately model the heat transfer mechanics which drive the mFFF process, the standard hot-end geometry needs to be included in the simulation domain to characterize its effect on melt behavior of mFFF. As previously stated, the underlying assumption of a homogeneous material must be thoroughly evaluated through experimental means. Finally, as is necessary for all numeric simulations, the model parameters need to be calibrated and the model predictions have to be validated using experimental data.

References

[1] S. Singh, G. Singh, C. Prakash, S. Ramakrishna, Current status and future directions of fused filament fabrication, Journal of Manufacturing Processes 55 (2020) 288–306. doi:https://doi.org/10.1016/j.jmapro.2020.04.049.

[2] J. Gonzalez-Gutierrez, S. Cano, S. Schuschnigg, C. Kukla, J. Sapkota, C. Holzer, Additive manufacturing of metallic and ceramic components by the material extrusion of highly-filled polymers: A review and future perspectives, Materials 11 (5) (2018) 840.

[3] J. Gonzalez-Gutierrez, I. Duretek, C. Kukla, A. Poljšak, M. Bek, I. Emri, C. Holzer, Models to predict the viscosity of metal injection molding feedstock materials as function of their formulation, Metals 6 (6) (2016). doi:10.3390/met6060129.

[4] M. M. Rueda, M.-C. Auscher, R. Fulchiron, T. Périé, G. Martin, P. Sonntag, P. Cassagnau, Rheology and applications of highly filled polymers: A review of current understanding, Progress in Polymer Science 66 (2017) 22–53, topical Volume on Polymer Physics. doi:https://doi.org/10.1016/j.progpolymsci.2016.12.007.

[5] L. M. Galantucci, A. Pellegrini, M. G. Guerra, F. Lavecchia, 3D printing of parts using metal extrusion: an overview of shaping debinding and sintering technology, Advanced Technologies and Materials 47 (1) (2022) 25–32.

[6] S. Hosseinimehr, A. Mohammadpanah, M. J. Benoit, D. F. Ester, A. Zang, M. Martinez, X. Jin, A. T. Clare, Defect evolution and mitigation in metal extrusion additive manufacturing: From deposition to sintering, Journal of Materials Processing Technology 329 (2024) 118457. doi:https://doi.org/10.1016/j.jmatprotec.2024.118457.

[7] D. Jiang, F. Ning, Physical-mechanical behaviors of stainless steel plate-lattice built by material extrusion additive manufacturing, Journal of Materials Processing Technology 309 (2022) 117739.

[8] F. Wang, S. You, D. Jiang, F. Ning, Study on sintering mechanism for extrusion-based additive manufacturing of stainless steel through molecular dynamics simulation, Additive

Manufacturing 58 (2022) 102991. doi:https://doi.org/10.1016/j.addma.2022.102991.

[9] N. K. Bankapalli, V. Gupta, P. Saxena, A. Bajpai, C. Lahoda, J. Polte, Filament fabrication and subsequent additive manufacturing, debinding, and sintering for extrusion-based metal additive manufacturing and their applications: A review, Composites Part B: Engineering 264 (2023) 110915. doi:https://doi.org/10.1016/j.compositesb.2023.110915.

[10] J. M. Costa, E. W. Sequeiros, M. F. Vieira, Fused filament fabrication for metallic materials: A brief review, Materials 16 (24) (2023). doi:https://doi.org/10.3390/ma16247505.

[11] S. Costa, F. Duarte, J. Covas, Estimation of filament temperature and adhesion development in fused deposition techniques, Journal of Materials Processing Technology 245 (2017) 167–179. doi:https://doi.org/10.1016/j.jmatprotec.2017.02.026.

[12] X. Gao, S. Qi, X. Kuang, Y. Su, J. Li, D. Wang, Fused filament fabrication of polymer materials: A review of interlayer bond, Additive Manufacturing 37 (2021) 101658. doi:https://doi.org/10.1016/j.addma.2020.101658.

[13] N. Ben Ali, M. Khlif, D. Hammami, C. Bradai, Experimental optimization of process parameters on mechanical properties and the layers adhesion of 3D printed parts, Journal of Applied Polymer Science 139 (9) (2022) 51706.

[14] A. A. Rashid, M. Koç, Fused Filament Fabrication process: a review of numerical simulation techniques, Polymers 13 (20) (2021) 3534.

[15] A. Bellini, S. Gu¨c¸eri, M. Bertoldi, Liquefier dynamics in fused deposition 126 (2) 237–246. doi:10.1115/1.1688377.

[16] M. AtifYardimci, T. Hattori, S. I. Guceri, S. C. Danforth, Thermal analysis of fused deposition (1997).

[17] J. Go, S. N. Schiffres, A. G. Stevens, A. J. Hart, Rate limits of additive manufacturing by Fused Filament Fabrication and guidelines for high-throughput system design, Additive Manufacturing 16 (2017) 1–11.

[18] D. D. Phan, Z. R. Swain, M. E. Mackay, Rheological and heat transfer effects in fused filament fabrication, Journal of Rheology 62 (5) (2018) 1097–1107.

[19] J. Zhang, B. Van Hooreweder, E. Ferraris, T4f3: temperature for fused filament fabrication, Progress in additive manufacturing. 7 (5) (2022-10). doi:https://doi.org/10.1007/s40964-022-00271-0.

[20] J. Zhang, E. Vasiliauskaite, A. De Kuyper, C. De Schryver, F. Vogeler, F. Desplentere, E. Ferraris, Temperature analyses in fused filament fabrication: From filament entering the hot-end to the printed parts, 3D Printing and Additive Manufacturing 9 (2) (2022) 132–142. doi:10.1089/3dp.2020.0339.

[21] A. Pellegrini, F. Lavecchia, M. G. Guerra, L. M. Galantucci, Influence of aging treatments on 17–4 ph stainless steel parts realized using material extrusion additive manufacturing technologies, The International Journal of Advanced Manufacturing Technology 126 (1) (2023) 163–178.

[22] M. Galati, P. Minetola, Analysis of density, roughness, and accuracy of the atomic diffusion additive manufacturing (adam) process for metal parts, Materials 12 (24) (2019). doi:10.3390/ma12244122.

[23] L. Waalkes, J. Längerich, P. Imgrund, C. Emmelmann, Piston-based material extrusion of ti-6al-4v feedstock for complementary use in metal injection molding, Materials 15 (1) (2022) 351.

[24] M. P. Serdeczny, R. Comminal, M. T. Mollah, D. B. Pedersen, J. Spangenberg, Numerical modeling of the polymer flow through the hot-end in filament-based material extrusion additive manufacturing, Additive Manufacturing 36 (2020) 101454.

[25] C. O. Ufodike, G. C. Nzebuka, Investigation of thermal evolution and fluid flow in the hot-end of a material extrusion 3d printer using melting model, Additive Manufacturing 49 (2022) 102502. doi:https://doi.org/10.1016/j.addma.2021.102502.

[26] A. A. Mishra, A. Momin, M. Strano, K. Rane, Implementation of viscosity and density models for improved numerical analysis of melt flow dynamics in the nozzle during extrusion-based additive manufacturing, Progress in Additive Manufacturing (2022) 1–14.

[27] D. F. Heaney, Handbook of Metal Injection Molding, Woodhead Publishing, 2018.

[28] K. H. Kate, R. K. Enneti, S.-J. Park, R. M. German, S. V. Atre, Predicting powder-polymer mixture properties for PIM design, Critical reviews in solid state and materials sciences 39 (3) (2014) 197–214.

[29] Flow Science, Inc., FLOW-3D, Version 2023R1, Santa Fe, NM (2023).
URL https://www.flow3d.com/

[30] C. Hirt, B. Nichols, Volume of fluid (VOF) method for the dynamics of free boundaries, Journal of Computational Physics 39 (1) (1981) 201–225. doi:https://doi.org/10.1016/0021-9991(81)90145-5.

[31] S. Li, K. Wang, J. Correia, Y. Liu, S. Ahzi, Investigating gradient temperature control for enhanced interfacial bonding behavior in material extrusion 3D printing continuous fiber reinforced polymer composites, European Journal of Mechanics-A/Solids (2024) 105349.

[32] S. Ahn, S. J. Park, S. Lee, S. V. Atre, R. M. German, Effect of powders and binders on material properties and molding parameters in iron and stainless steel powder injection molding process, Powder Technology 193 (2) (2009) 162–169. doi:https://doi.org/10.1016/j.powtec.2009.03.010.

Response to Reviewers' Comments

Reviewer 1	
Comment:	**Response:**
1) ASTM standard term is "additively manufactured", please use in place of "3d printed", as this better reflects the nature of the process.	Resolved as requested.
2) Figure and table labels should be included below, not above	Resolved as requested.
3) Don't need to hyphenate words at line end, word will self-correct when using justified text	Resolved as requested.
Reviewer 2	
Comment:	**Response:**
4) In several places, words were intentionally hyphenated at the end of lines. The justified format in MS word and other text programs will automatically adjust this, so hyphens are not needed and should be removed	Resolved as requested.
5) Claims in introduction could use sources	More references have been added in the Introduction section. "The shape of the raster determines the contact area between deposited material, which then affects the macro-scale part strength [12, 13]" – [13] Gao et al., 2021 "A comprehensive review of mFFF process can be found in Bankapalli [9] and Costa [10]." – [10] Costa et al. , 2023 "The current state of numeric modeling for the FFF process predominantly focuses on homogeneous polymers. [1, 19, 20]" -[19] Zhang et al. - 2022 -[20] Zhang et al. - 2022
6) Grammar and spelling errors are present in multiple places, please proofread paper and correct these	Related errors have been corrected.
7) Reference numbers are colored differently from the rest of the manuscript, please correct to all black text	Resolved as requested.
8) Check that manuscript format matches formatting required for conference	Resolved as requested

9) The term “3d printed” is used in a couple places. The ASTM standard terminology is “additive manufacturing”, this term or a derivative of it should be used instead of “3d printing”, as it gives a more correct reflection of the nature of the technology	Resolved as requested.
10) Figure and table labels should be included below the figures or tables, check manuscript and correct	Format issue resolved as requested.
Reviewer 3	
Comment:	**Response:**
11) "The shape of the raster then affects the macro-scale part strength of the part [10]." Repeated use of the word "part".	The typo has been resolved as requested.
12) There is room to add more references related to prior modeling efforts to strengthen the motivation for the current work.	See response to comment 5.
13) “The fluid source in the model is defined to maintain a user defined temperature (note).” Clarify what note refers to in this sentence.	The typo has been removed.
14) Please clarify that rule of mixtures is used to evaluate the properties when discussing model setup and related equations. This was mentioned in the Results and Discussion section.	The use of the rule of mixtures is discussed in the *Computational Domain* section with the following text: “The material approximations for the FFF filament are assumed to be similar to the metal injection molding feedstock and are approximated through the rule of mixtures approach. The properties of a composite material (A_f) can be approximated from its constituent materials and their respective volume fractions as shown in Eq. 1 .”
15) Showing the equations and boundary conditions in Figure 1 would make the model setup clearer and easy to follow.	This figure is intended to be a general view of the metal fused filament fabrication process. We prefer to elaborate on the related equations and boundary conditions in the text, to keep the figure simple.
16) Providing geometry-related parameters in Figure1 would improve readability.	See response to comment 15. Geometry related parameters are explained in the text following Figure 1.
17) “Finally, Eqs. 10,11, and 12estimate the thermal state of the fluid within each	Spacing was resolved as requested

cell." Spacing between 12 and estimate must be corrected.	
18) It is unclear if any calibration is involved.	The final sentence of the conclusion was reworded to address the reviewer's comment. "Finally, as is necessary for all numeric simulations, the model parameters need to be calibrated and the model predictions have to be validated using experimental data."
19) Provide mesh and timestep details.	The following sentence has been updated in the *Results and Discussion* section to provide the details. "A global mesh size of 0.1 mm was evaluated at a minimum timestep of $3x10^{-10}$s "
20) "For the fastest speed (50mm/s) the deposited material retains heat even when the nozzle has moved away further. The residual heat after deposition induces further Thermal shrinkage." This could be the result of thermal gradients magnitude and not necessarily the residual heat. If anything, residual heat should minimize the stress due to slow cooling. The authors are requested to revisit the residual stress origins and clarify the discussion further.	We agree with the reviewer and intend to perform further analysis on the effect of cooling rates on residual stresses. The following phrase has been updated in the *Results and Discussion* section to address the reviewer's comment. "For the fastest speed (50 mm/s) the deposited material retains heat even when the nozzle has moved away further. The increased area of higher temperatures can be advantageous or detrimental to the part-scale process. If the next or adjacent layer is deposited before the current layer cools, the residual heat benefits diffusion across layer boundaries. If the deposited layer is allowed to cool to ambient temperature, the increased area of higher temperature leads to increased thermal shrinkage and decreases interfacial bond strength."
21) "This suggests that faster print speeds will be subject to sharper thermal gradients when exposed to ambient temperature." This statement in the conclusions section contrasts with the following statement in the discussion section. "The slower print speeds demonstrate sharper internal thermal gradient compared to the faster print speeds."	The statement has been corrected in the *Results and Discussions* section of the revised manuscript. "The slower print speeds demonstrate a less severe internal thermal gradient than the faster print speeds."

22) Equation 13 is a convection heat transfer equation. The use of it as an energy source rate is unclear.	Equation 13 is used to model the heat transfer between walls and fluid within the simulation. This preliminary model assumes pure convection for fluid-structure interactions. The discussion of equation 13 has been updated to the following: “The local heat transfer between the walls of the domain, such as the build-plate, and the fluid is evaluated as a function of wall temperature in the linear relationship shown in Eq. 13”